COVER SHEET

Title: *Numerical Predictions of Damage and Failure in Carbon Fiber Reinforced Laminates Using a Thermodynamically-Based Work Potential Theory* Proceedings of the **American Society for Composites Twenty-Eight Technical Conference**

Authors: Evan J. Pineda
Anthony M. Waas

ABSTRACT

A thermodynamically-based work potential theory for modeling progressive damage and failure in fiber-reinforced laminates is presented. The current, multiple-internal state variable (ISV) formulation, referred to as enhanced Schapery theory (EST), utilizes separate ISVs for modeling the effects of damage and failure. Consistent characteristic lengths are introduced into the formulation to govern the evolution of the failure ISVs. Using the stationarity of the total work potential with respect to each ISV, a set of thermodynamically consistent evolution equations for the ISVs are derived. The theory is implemented into a commercial finite element code. The model is verified against experimental results from two laminated, T800/3900-2 panels containing a central notch and different fiber-orientation stacking sequences. Global load versus displacement, global load versus local strain gage data, and macroscopic failure paths obtained from the models are compared against the experimental results.

INTRODUCTION

Development of accurate, predictive progressive damage and failure analysis (PDFA) tools is imperative for further advancement of composite structures. As the predictive capability of PDFA tools improves the potential design space for a composite component is expanded. Physical testing of materials and components will always be the most crucial aspect of design validation; however virtual testing can help focus, and reduce, the necessary testing on only the most promising designs. To meet the predictive requirements needed for virtual

Evan J. Pineda, Aerospace Research Engineer, Mechanics and Life Prediction Branch, NASA Glenn Research Center, 21000 Brookpark Rd., Cleveland, OH 44135.
Anthony M. Waas, Felix Pawlowski Collegiate Professor, Department of Aerospace Engineering, University of Michigan, Ann Arbor, MI 48109.

testing, a PDFA tool must be numerical objective and must incorporate the physics of the underlying damage and failure mechanisms in the composite.

A thermodynamically-based, work potential theory, known as Schapery theory (ST), was developed for modeling matrix microdamage in fiber-reinforced laminates (FRLs)[1, 2, 3, 4]. With ST, a single ISV is used to mark the degree of microdamage in the material. However, separate microdamage functions are employed to degrade the transverse and shear moduli, yielding coupled anisotropic damage evolution. [5] and [6] extended the formulation to include the effects of transverse cracking by adding an additional ISVs and predicted the evolution of microdamage and transverse cracking in coupon laminates analytically. [7] implemented this extended formulation in a numerical setting to simulate the failure of a buffer strip-reinforced, center-notched panel (CNP). However, due to the cumbersome nature of the evolution equations, the microdamage and transverse cracking evolution equations were decoupled to arrive at a more efficient implementation. Since no characteristic length is introduced into the formulation, the theory produces mesh-dependent results in a computational setting.

The ST formulation is further extended here, resulting in the enhanced Schapery theory (EST), to include the effects of macroscopic transverse and shear matrix cracking, as well as fiber breakage, using an approach that differs from [5, 6, 7]. A deliberate distinction between damage and failure is made in the theory. The traditional ISV used in ST is maintained to model microdamage.

Upon failure initiation, the element domain is no longer considered a continuum, and a smeared crack approach is used to model the embedded discontinuities [8, 9]. Three new ISVs, which incorporate the characteristic length of the finite element and operate similar to traditional tensorial damage variables, dictate the directional evolution of the failure due to fiber breakage and transverse cracking mechanisms. Since EST is implemented within FEM, transverse cracking is considered a discrete phenomenon leading immediately to failure at the element scale (i.e., one macroscopic crack per element). This does not, however, preclude the progressive evolution of cracks at the global scale that has been demonstrated to occur in multi-angle laminates [10]. The EST formulation presented herein offers non-linear progressive damage coupled with mesh objective, post-peak strain softening. EST incorporates physics-based methods for controlling the damage evolution within the material by using the measured relationships between transverse/shear degradation and the dissipated potential resulting from matrix microdamage. Moreover, failure evolution is governed by the material fracture toughness associated with fiber breakage and transverse cracking.

Finally, EST is verified against experimental results for two center-notched panels (CNPs). Global load versus deflection data, local strain gage data, as well as observed failure mechanisms obtained from experiments performed at the NASA Langley Research Center (LaRC) and reported in [11, 12] are compared to numerical results.
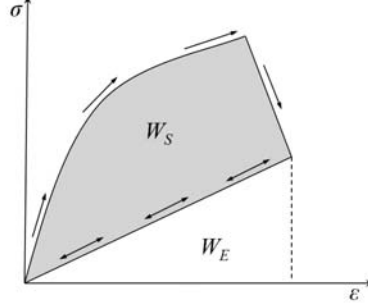
Figure 1. Typical stress-strain curve, containing pre-peak nonlinearity and post-peak strain softening, showing the total elastic (W_E) and total dissipated (W_S) potentials.

ENHANCED SCHAPERY THEORY

The previously developed ST ([3, 6, 7, 13, 14, 15]) is extended to accommodate mesh objective, post peak strain softening. Separate ISVs are used to govern the evolution of matrix microdamage, transverse (mode I) matrix failure, shear (mode II) matrix failure, and fiber breakage (mode I). The first and second laws of thermodynamics are enforced, establishing thermodynamically consistent evolution laws for progressive matrix microdamage, as well as post-peak failure. The following sections give a brief overview of the formulation of this work potential theory. For complete details, please refer to [16, 17, 18]

Thermodynamically-based Work Potential Framework

As a material is loaded, a measure of the work potential facilitates modeling structural changes in the material, such as microcracking, which affect the elastic properties of the material. Energy that is not dissipated is recovered when the structure is unloaded, and the magnitude of energy recovered is contingent upon the degraded, elastic properties at the previously attained maximum strain state. It is assumed, upon subsequent reloading, that the material behaves linearly, exhibiting the elastic properties observed during unloading, until the material reaches the preceding maximum strain state. After this state is achieved, structural changes resume, affecting degradation of the instantaneous elastic moduli of the material. This process is shown in the uniaxial stress-strain curve displayed in Figure 1. The shaded area above the unloading line represents total dissipated potential W_S, and the triangular area underneath is the total elastic strain energy density W_E. It is assumed that the material behaves as a secant material and there is no permanent deformation upon unloading. This a reasonable assumption for FRLs [5]; however, plastic deformation can also be incorporated, if necessary [3]. Extension to treat viscoelastic and viscoplastic response is outlined in [19].

Both W_E and W_S are functions of a set of ISVs, $S_m, (m = 1, 2, M)$. These ISVs account for any inelastic structural changes in the material. It is shown in

[2, 3] that the total work potential is stationary with respect to each ISV.

$$\frac{\partial W_T}{\partial S_m} = 0 \tag{1}$$

Additionally, [20] utilized the second law of thermodynamics to establish the inequality:

$$\dot{S}_m \geq 0 \tag{2}$$

where the overdot represents a time derivative and suggests that "healing" is not allowed for a material undergoing structural changes. Equations (1) and (2) form the foundation of a thermodynamically-based work potential theory for modeling non-linear structural changes in a material exhibiting limited path-dependence.

Multiple ISV Formulation of ST to Account for Multiple Damage and Failure Mechanisms

Due to the generality of the evolution equations, Equations (1) and (2), the work potential theory can account for any number and type of structural changes that may occur in a material. This is especially useful for modeling progressive damage in composites because the heterogeneity of the composite, and multiaxiality of the local fields, enables multiple damage mechanisms to arise during a typical loading history.

The present EST formulation assumes that three major intralaminar mechanisms are responsible for all observed non-linearities in the stress-strain curve of a composite lamina: matrix microdamage, matrix macroscopic cracking, and axial fiber failure. Each of these mechanisms can be accommodated by partitioning the total dissipated energy density, W_S, into portions associated with each mechanism. Although delamination is a prominent failure mechanism in laminated composites, theories and methods to address this mechanism have been developed to a fairly mature state [21, 22]. The authors have left the coupling of in-plane and out-of-plane damage mechanisms as a future exercise involving the placement of cohesive zone elements between plies, yet recent preliminary results have been promising [23].

It has been reported that, under tension at room temperature, thermoset epoxy matrix composites exhibit minimal plastic deformation or viscous effects[1, 5]. Thus, matrix microdamage is the primary cause of observed non-linearity in the stress versus strain response of many polymer matrix composites (PMCs) up to localization of microdamage into more severe failure mechanisms, such as transverse cracking, fiber breakage, kink band formation, or delamination. Microdamage can be considered as the combination of matrix microcracking, micro-void growth, shear banding, and fiber-matrix debonding. Figure 2 shows a typical uniaxial response of a material exhibiting microdamage evolution, where the recoverable energy potential is given by W and the potential dissipated into evolving structural changes associated with microdamage is given by S.
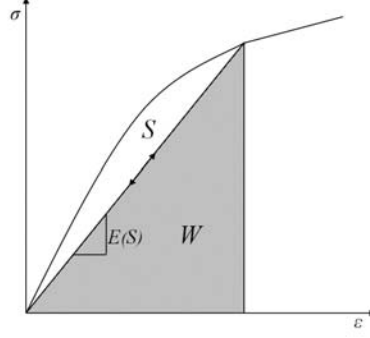
Figure 2. Typical stress-strain curve with a positive-definite tangent stiffness exhibiting microdamage, showing the elastic (W) and irrecoverable (S) portions.

Typically, matrix microdamage continues to grow until the onset of more catastrophic failure mechanisms initiate. It should be noted that we have explicitly distinguished between damage and failure in the following manner:

Damage - Structural changes in a material that manifest as pre-peak non-linearity in the stress-strain response of the material through the degradation of the secant moduli.

Failure - Structural changes that result from damage localization in a material and manifest as post-peak strain softening in the stress-strain response of the material.

It is noted that this demarcation is not inclusive nor unique with respect to other types of phenomena in a broad range of materials that can also affect the secant moduli. The purpose here is to clearly point out demarcations with respect to the pre-peak (positive tangent stiffness) and post-peak (non-positive tangent stiffness) regime observed in matrix dominated damage and failure as it applies to fiber reinforced polymer matrix composites.

These demarcations of damage and failure differ slightly from those typically used in previous works. Often, damage would be defined as any phenomena that affected the secant stiffness of the material (regardless of whether it yielded a positive or negative tangent stiffness), and failure was considered the final point on a stress-strain curve, after which, the stress would drop suddenly to zero[24, 25, 26, 11, 27, 28, 29, 30]. By partitioning damage and failure, as specified in this work, a characteristic length can be introduced into the formulation of the failure evolution, as necessary, while the damage evolution can remain independent of the size.

Here, three major failure mechanisms, which are distinct from the microdamage modes, are considered: transverse (mode I) matrix cracking, shear (mode II) matrix cracking, and axial (mode I) fiber fracture. These failure modes are consistent with the in-plane failure typically observed in PMC laminates. It is assumed that the evolution of these mechanisms yields an immediate reduction in the load-carrying capability of a local subvolume where the mechanism is active. Three ISVs are used to account for mode I matrix cracking, mode II matrix

cracking, and mode I fiber failure, respectively: S_I^m, S_{II}^m, and S_I^f. These ISVs are defined completely in a later section, and are taken to be the potentials required to advance structural changes associated with these failure mechanisms.

At any given state, the total dissipated energy density, W_S, can be calculated as a sum of energy dissipated through the aforementioned damage and failure mechanisms, given by the four ISVs.

$$W_S = S + S_{IF}^m + S_{IIF}^m + S_I^f \tag{3}$$

According to the first law of thermodynamics, the total work potential (ignoring thermal dissipation) is given by the sum of the elastic strain energy density and the potentials associated with each of the damage or failure mechanisms.

$$W_T = W_E + S + S_I^m + S_{II}^m + S_I^f \tag{4}$$

where W_E is the elastic strain energy density. Invoking the stationarity principle, Equation (1),

$$\frac{\partial W_E}{\partial S} = -1 \quad \frac{\partial W_E}{\partial S_I^f} = -1$$

$$\frac{\partial W_E}{\partial S_I^m} = -1 \quad \frac{\partial W_E}{\partial S_{II}^m} = -1 \tag{5}$$

and the Second Law of Thermodynamics, Equation (2), gives:

$$\dot{S} \geq 0 \quad \dot{S}_F^f \geq 0$$

$$\dot{S}_{IF}^m \geq 0 \quad \dot{S}_{IIF}^m \geq 0 \tag{6}$$

Equations (5) and (6) constitute the evolution equations for damage and failure in a material associated with matrix microdamage, matrix cracking, and fiber breakage in tension.

Use of Traction-Separation Relationships to Define the Failure Potentials

In the previous publications [5, 6, 7], it was assumed that the transverse cracking affected the relationships between stress and strain. However, the existence of a macroscopic crack invalidates the assumption of a continuum. Here, it is presumed that failure arises from the evolution of cohesive cracks within the continuum, and the ISVs associated with failure (axial, transverse, and shear) influence the relationship between traction on the crack faces and the crack-tip opening displacement. The satisfaction of a Hashin-Rotem (H-R) failure criterion [31] indicates the material behavior transitions from that of a damaging continuum to that of a cohesive crack, and the essential fields become traction and separation, rather than stress and strain (see Figure 3).

Once a cohesive crack initiates in the continuum, opening of the crack yields a reduction in traction on the crack faces at the crack tip, [32]. If subsequently
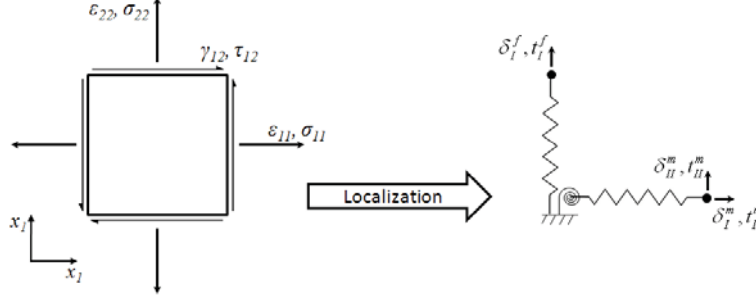
Figure 3. Schematic showing the transition form a continuum to a cohesive zone due to the initiation of macroscopic cracks. The essential, constitutive variables switch from stress and strain to traction and separation.

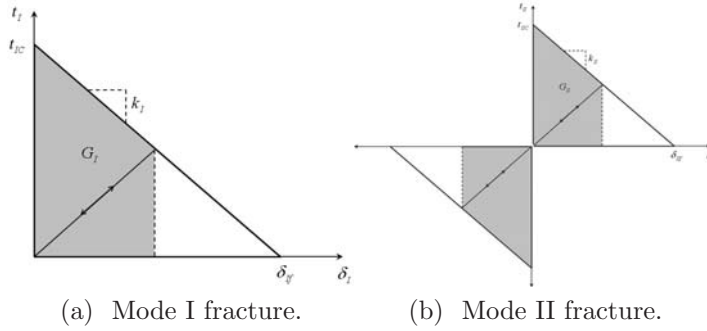(a) Mode I fracture. (b) Mode II fracture.

Figure 4. Triangular traction versus separation which dictates the behavior of cohesive cracks embedded in the continuum. The total area under the traction-separation law represents the material fracture toughness G_{mC}^{j}.

the crack is closed, it is assumed that traction at the crack tip will unload linearly towards the origin of the traction versus separation law (see Figure 4). The strain energy release rate (SERR) G_M^j is calculated as:

$$G_M^j = \oint t_M^j d\delta_M^j \tag{7}$$

where j indicates the material (fiber f or matrix m), M represents the corresponding mode (mode I or mode II), δ_M^j is the crack tip opening displacement in mode M and material j, and t_M^j is the corresponding traction at the crack tip.

It should be noted, the traction-separation laws exhibited in Figure 4 do not require any initial, fictitious, pre-peak stiffness because the cracks are embedded within a continuum. This is an advantage over the use of DCZM elements which do require an initial stiffness because these interfacial elements do not actually represent physical material within the model and must attempt to simulate initially perfect bonding between adjacent material domains [33, 34]. If set incorrectly, these fictitious stiffnesses can cause numerical problems [35].

Using the traction-separation laws in Figure 4 and assuming the cracks are not closing, the dissipation potentials in an element resulting from macroscopic

cracking are related to the SERRs using suitable element dimensions and removing the energy potential that may be recovered upon closing of the crack.

$$S_I^f = \frac{G_I^f}{l_e^{(\theta+90°)}} - \frac{t_I^f \delta_I^f}{2l_e^{(\theta+90°)}}, \quad S_I^m = \frac{G_I^m}{l_e^{(\theta)}} - \frac{t_I^m \delta_I^m}{2l_e^{(\theta)}}, \quad S_{II}^m = \frac{G_{II}^m}{l_e^{(\theta)}} - \frac{t_{II}^m \delta_{II}^m}{2l_e^{(\theta)}}, \qquad (8)$$

where, $l_e^{(\theta+90°)}$ is the length of a line running perpendicular to fiber direction in the element that intersects two edges of the element and the integration point, and $l_e^{(\theta)}$ is the length of a line that is parallel to the fiber direction in the element that intersects two edges of the element and the integration point.

EST Evolution Equations for a Fiber-Reinforced Lamina

To arrive at the evolution equations for the four ISVs, the elastic strain energy density must be defined for a material which may contain cohesive cracks. Therefore, the elastic strain energy W_E is comprised of a contribution from the continuum W and any possible cohesive cracks W_M^j. The plane stress, elastic strain energy density in the continuum is defined as

$$W = \frac{1}{2}(E_{11}\epsilon_{11}^2 + E_{22}(S)\epsilon_{22}^2 + G_{12}(S)\gamma_{12}^2) + Q_{12}\epsilon_{11}\epsilon_{22} \qquad (9)$$

where stress in the laminae are related to strain assuming plane stress conditions [36].

Note that only the transverse and shear moduli (E_{22} and G_{12}) are functions of S since matrix microdamage only accrues in the matrix of the laminae. The Poisson's ratio is assumed to evolve such that the quantity $Q_{12} = E_{22}\nu_{12}$ remains constant; however, this restriction can be relaxed if deemed necessary. The degraded moduli are related to the virgin moduli (E_{220} and G_{120}) and the ISV through a set of microdamage functions ($e_s(S)$ and $g_s(S)$) that are obtained from three uniaxial coupon tests [2, 5, 6].

$$E_{22} = E_{220}e_s(S) \qquad (10)$$

$$G_{12} = G_{120}g_s(S) \qquad (11)$$

Degrading E_{22} and G_{12} exclusively is consistent with the intralaminar damage typically observed in PMC laminates.

The elastic strain energy density of the cohesive cracks are defined as the recoverable energy per unit crack surface area smeared over the entire element.

$$W_I^f = \frac{t_I^f \delta_I^f}{2l_e^{(\theta+90°)}} \qquad (12)$$

$$W_I^m = \frac{t_I^m \delta_I^m}{2l_e^{(\theta)}} \qquad (13)$$

$$W_{II}^m = \frac{t_{II}^m \delta_{II}^m}{2l_e^{(\theta)}} \qquad (14)$$

Substituting Equations (9) - (11) into Equation (5) gives the evolution equation for the microdamage ISV.

$$\frac{1}{2}\left(\epsilon_{22}^2 E_{220}\frac{de_s}{dS_r} + \gamma_{12}^2 G_{120}\frac{dg_s}{dS_r}\right) = -3S_r^2 \tag{15}$$

The use of a reduced ISV $S_r = S^{\frac{1}{3}}$ has been employed in Equation (15). [5] has shown that the use of this reduced ISV yields polynomial forms of the microdamage functions in Equations (10) and (11). Thus, Equation (15) becomes a polynomial equation that can be readily solved for S_r for a given strain state $(\epsilon_{22}, \gamma_{12})$.

Once failure initiates, the effects of failure supersede the effects of microdamage and evolution of S ceases. The triangular traction-separation laws (see Figure 4) can be employed to evaluate Equations (12)-(14), then they can be substituted into Equations (5), which can be solved for the degraded moduli of the lamina.

$$E_{11} = \left\{\frac{1}{E_{110}} - \frac{\epsilon_{11} - \epsilon_{11}^C}{t_{IC}^f\left[1 + \frac{l_e^{(\theta+90°)}t_{IC}^f}{2G_{IC}^f}\left(\epsilon_{11} - \epsilon_{11}^C\right)\right]}\right\}^{-1} \tag{16}$$

$$E_{22} = \left\{\frac{1}{E_{22}^*} - \frac{\epsilon_{22} - \epsilon_{22}^C}{t_{IC}^m\left[1 + \frac{l_e^{(\theta)}t_{IC}^m}{2G_{IC}^m}\left(\epsilon_{22} - \epsilon_{22}^C\right)\right]}\right\}^{-1} \tag{17}$$

$$G_{12} = \left\{\frac{1}{G_{12}^*} - \frac{\gamma_{12} - \gamma_{12}^C}{2t_{IIC}^m\left[1 + \frac{l_e^{(\theta)}t_{IIC}^m}{4G_{IIC}^m}\left(\gamma_{12} - \gamma_{12}^C\right)\right]}\right\}^{-1} \tag{18}$$

where E_{22}^* and G_{12}^* are the degraded transverse and shear moduli, due to microdamage, when the H-R criterion is satisfied.

To transition from crack tip opening displacement to integration point strain (which is needed to perfrom the calculations at an integration point within a FEM model), it is assumed that following failure initiation the strains are related to the crack tip opening displacements by

$$l_e^{(\theta+90°)}\epsilon_{11} = l_e^{(\theta+90°)}\epsilon_{11}^C + \delta_I^f \tag{19}$$

$$l_e^{(\theta)}\epsilon_{22} = l_e^{(\theta)}\epsilon_{22}^C + \delta_I^m \tag{20}$$

$$l_e^{(\theta)}\gamma_{12} = l_e^{(\theta)}\gamma_{12}^C + 2\delta_{II}^m \tag{21}$$

where ϵ_{11}^C, ϵ_{22}^C, and γ_{12}^C are the strains when the H-R failure criterion is satisfied. Equations (19)-(21) imply that the strain in the continuum remains at the values obtained when failure initiates, and that any incremental change in the global strain after failure initiation is used wholly to advance the crack tip opening displacement.

The negative tangent stiffness of the stress-strain response necessary for post-peak strain softening to occur imposes a restriction on the maximum allowable element size, as shown by [8].

$$l_e^{(\theta+90^\circ)} < \frac{2G_{IC}^f E_{11}}{t_{IC}^{f}{}^2} \tag{22}$$

$$l_e^{(\theta)} < \min\left\{\frac{2G_{IC}^m E_{22}^*}{t_{IC}^{m}{}^2}, \frac{2G_{IIC}^m G_{12}^*}{t_{IIC}^{m}{}^2}\right\} \tag{23}$$

The analyst must be careful to ensure the dimensions of any failing elements are smaller than the conditions given in Equations (22) and (23).

In summary, the satisfaction of the H-R failure criterion marks the transition from evolving microdamage to failure to macroscopic cracking. Prior to failure initiation, Equation (15) is used to calculate the microdamage reduced ISV S_r, and the failure ISVs S_I^f, S_I^m, and S_{II}^m remain zero. Equations (10) and (11) are used to calculate the degraded transverse and shear moduli. Subsequent to matrix failure initiation, microdamage growth is precluded, and S_r remains at S_r^*, the value of S_r when the H-R criterion for the matrix was satisfied. The degeneration of the transverse and shear moduli, resulting from matrix transverse and shear cracking, is calculated using Equations (17) and (18). Finally if the H-R criterion for the fiber is satisfied, the axial modulus is calculated using Equations (16) as fiber breakage evolves in the element. Once the material moduli have been calculated using the appropriate evolution equations, the stresses can be updated accordingly.

EXAMPLE - CENTER NOTCHED PANELS SUBJECTED TO UNIAXIAL TENSION

Experimental Details

Two center-notched panel (CNP) configurations were tested at the NASA Langley Research Center (LaRC) [11, 12]. The geometrical details of the panel and testing boundary conditions are presented in Figure 5. End tabs affixed to the panel were clamped and a vertical, tensile displacement (in the y-direction) was applied to the top tab using a servo-hydraulic testing machine. The bottom tab was fixed preventing any y-displacement of the bottom boundary of the gage section. The gripped tabs also prevented any displacement in the x-direction at the top and bottom boundaries of the gage section.

The panels were comprised of laminated T800/3900-2 carbon fiber/toughened epoxy composites. Three different lay-up configurations were tested; however one of the configurations exhibited significant delamination. Since the focus of
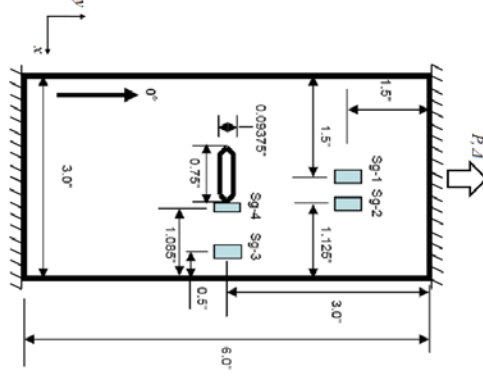
Figure 5. Geometry, boundary conditions, and strain gage (Sg) locations of CNPs tested at NASA LaRC [11].

TABLE I. T800/3900-2 LAY-UP CONFIGURATIONS USED IN CNP TESTS AT NASA LaRC.

ID	Stacking Sequence	Thickness (in.)
Laminate-1	$[0°]_{12}$	0.078
Laminate-2	$[45°/0°/-45°/0°/90°]_S$	0.065

this work is modeling in-plane damage and failure mechanisms, this configuration is not considered here. The two remaining configurations are presented in Table I. The first lay-up, Laminate-1, consists of twelve 0° plies, and the second, Laminate-2, is a symmetric, multi-angle lay-up with 40% of |45°|, 40% of 0°, and 20% of 90° laminae.

Several strain gages where affixed to the test panel, labeled Sg-1 through Sg-4 in Figure 5. Sg-1 was placed in the center of the panel, 1.5" above the notch. Sg-2 was placed 1.5" above the notch tip. Sg-3 was attached in front of the notch, 0.5" from the free edge, and Sg-4 placed at the notch tip. Global load versus displacement data, and local strain gage data were reported in [11, 12], along with a post-test C-Scan of Laminate-1 and photograph of Laminate-1 and photograph of Laminate-2.

Finite Element Model Details

EST was integrated into the Abaqus FEM software using the user material Fortran subroutine UMAT[37]. The linear elastic properties of T800/3900-2 used in the FEM models were taken from [11]. The shear microdamage function g_s utilized in Equation (11) was obtained from the shear stress-shear strain (τ_{12}-γ_{12}) response of $[45°/-45°]_{3S}$ angle-ply T800/3900-2 coupon tests as recommended by [5]. The transverse, tensile and compressive microdamage functions were inferred by scaling the coefficients of the microdamage curves presented by [5] for AS4/3502 by the ratio of the virgin transverse modulus of T800/3900-2 to that of AS4/3502, as the stress-strain curves of the T800/3900-2 coupon laminates necessary to characterize e_s were not available. The microdamage curves are presented in Figure 6.
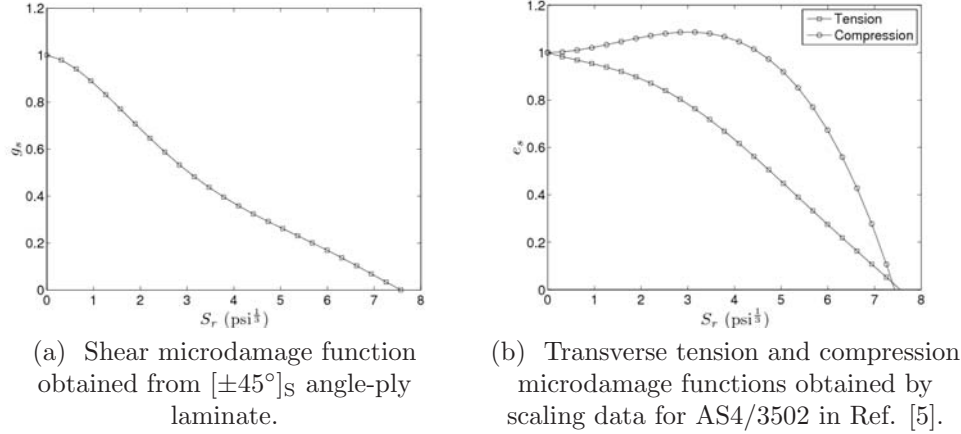
(a) Shear microdamage function obtained from $[\pm 45°]_S$ angle-ply laminate.

(b) Transverse tension and compression microdamage functions obtained by scaling data for AS4/3502 in Ref. [5].

Figure 6. Microdamage functions for T800/3900-2 used in FEM models.

TABLE II. FAILURE PARAMETERS FOR T800/3900-2.

Property	Value	Property	Value
X_T	0.021	G_{IC}^f	1026 $\frac{\text{lbf.-in.}}{\text{in.}^2}$
Y_T	0.0092	G_{IC}^m	2.39 $\frac{\text{lbf.-in.}}{\text{in.}^2}$
Z	0.0075	G_{IIC}^m	6.78 $\frac{\text{lbf.-in.}}{\text{in.}^2}$

The axial mode I, transverse mode I, and shear mode II critical cohesive strains, and fracture toughness' are given in Table II. The matrix mode II cohesive critical strains (Z) and the fracture toughnesses (G_{IIC}^m) were calibrated using data from Laminate-1. The critical strains were estimated using the ratio of the matrix strengths of IM7/8552, [38] and the calibrated critical shear strain in Table II. It was assumed that the characteristic material length of the mode I transverse crack band mechanism of T800/3900-2 and IM7/8552 were comparable. Thus, the ratio of the mode I matrix fracture toughness to the strength squared was multiplied by the assumed critical mode I matrix strain and the transverse modulus to arrive at the value of G_{IC}^m used in the simulations and tabulated in Table II. Laminate-1 did not exhibit any axial failure; so, the fiber mode I parameters (X_T and G_{IC}^f) were calibrated such that the ultimate load from the simulation of Laminate-2 corresponded with the ultimate load reported by [11] for Laminate-2.

Results - Laminate-1

Global load P versus displacement Δ of a 4" section of Laminate-1 is compared to results from the EST simulation in Figure 7. Very good agreement between the model and the experimental results is achieved. The response of the specimen appears to be linear until near 8,000 lbf., where the specimen begins deforming non-linearly. The EST simulation captures the initiation and progression of the global nonlinearity accurately. This panel was not loaded

until catastrophic failure; hence, the data presented in Figure 7 represents load versus displacement data prior to the ultimate load of the specimen.
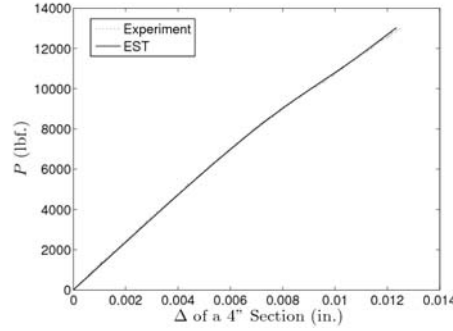

Figure 7. Applied load versus displacement of a 4" section for Laminate-1.

Local strain gage data (global load P versus local y-direction strain ϵ_{yy}) from Laminate-1 is plotted with the results from the EST FEM model in Figure 8; refer to Figure 5 for locations of strain gages. Strain relaxation is observed in the gage farthest away from the notch: Sg-1, shown in Figure 8a. The mode I and mode II matrix failure parameters in EST were calibrated such that the model demonstrates the same transition into strain relaxation at this location and at a similar global applied load. This load, taken as the splitting load, is 8,250 lbf. in the experiment and 8,210 lbf. in the model. The transition to strain relaxation is more abrupt in the experiment as evidenced by the sharp knee in the load-strain curve, whereas, the transition in the model is more gradual.

The data from the experiment and simulation for Sg-2, which is located 1.5" directly above the notch, are presented in Figure 8b. The model predicts less strain at Sg-2, for a given load, than the experiment, but the non-linear trends are very similar. This gage lies directly in front of the splitting crack path, shown in Figure 5, and it is not realistic to expect perfect agreement in areas experiencing high levels of damage and failure because of idealizations used to model the evolution of cracks in the simulations.

Figure 8c displays data for Sg-3, located in front of the notch near the free edge. Very good agreement between the experimental and simulation results are exhibited. The model accurately captures the non-linear evolution of strain, away from the highly damaged regions, as a function of applied load.

Finally, results for Sg-4 (located directly at the notch tip) are given in Figure 8d and includes the experiment and simulation display of axial strain relaxation. As with Sg-2, Sg-4 shows less strain for a given applied load. However, the load at which the strain at Sg-4 relaxes in both the experiment and model correlate well, in accordance with the splitting load. Again, the relaxation response of the experiment is discontinuous, but the model exhibits continuous behavior.

A C-Scan of the failed Laminate-1 specimen is displayed in Figure 9. Four splitting cracks can be observed, shown in green, propagating outward from the notch tip, parallel to the loading direction, towards the gripped edges. Contour plots of the normalized microdamage obtained from the simulation are presented
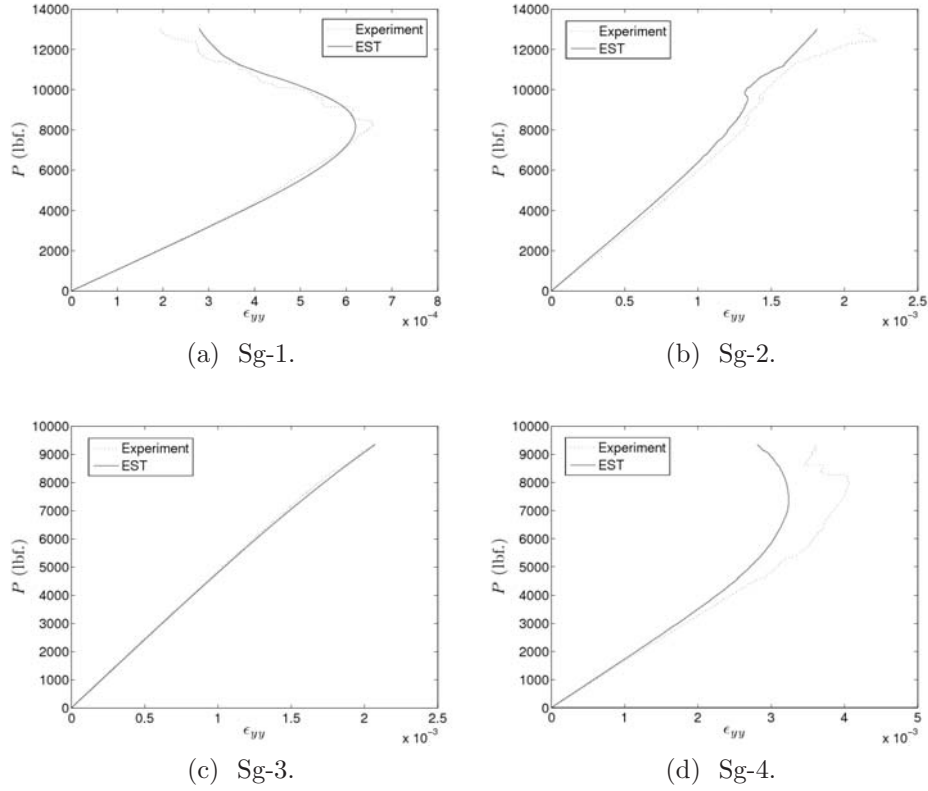
(a) Sg-1.　　　　　　　　　　　　　(b) Sg-2.

(c) Sg-3.　　　　　　　　　　　　　(d) Sg-4.

Figure 8. Applied load versus local strain for Laminate-1.

in Figure 10a at 16,400 lbf. In these plots, S_r is normalized by the maximum achievable value. The regions of maximum damage are localized to small regions, along the same crack path observed in Figure 9, embedded in a more widespread domain and exhibiting less severe microdamage. Figure 10b shows the shear failure degradation factor D_{II}^m at 16,400 lbf. The shear failure localizes into crack bands that are a single element wide and progress equivalently to the splitting cracks observed in the experiment.

Results - Laminate-2

Numerical results for applied load versus displacement of a 4" section of Laminate-2 are presented in Figure 11. The experimental ultimate load 15,300 lbf. correlates well (axial failure parameters were calibrated to obtain an ultimate load that most closely matched the experimental data) with the ultimate load obtained from the model, also 15,300 lbf.. The global response up to failure is nearly linear and failure occurs suddenly and catastrophically.

Figure 12 compares the applied load versus strain gage results from the model to the data from the experiment. Sg-1 and Sg-2 exhibited similar behavior; the strain increases until the ultimate load is obtained, after which the strain relaxes abruptly. The experimental data and numerical results both display
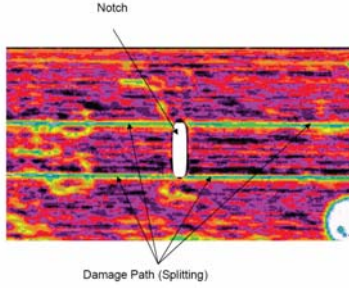
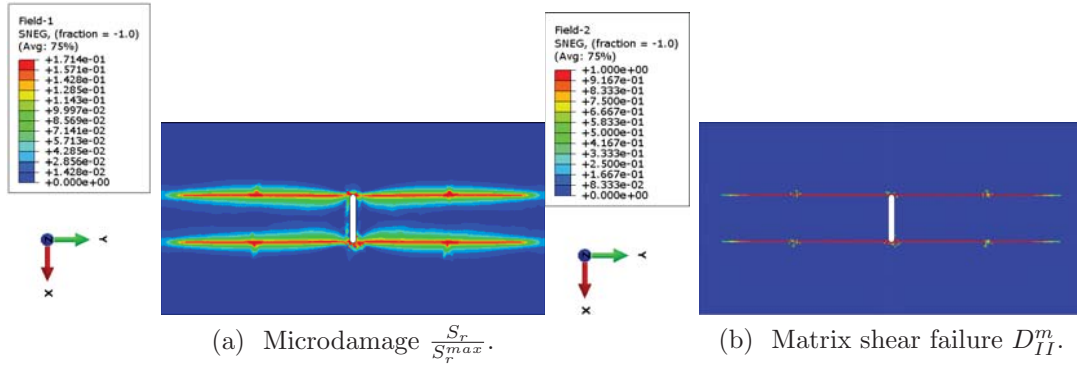Figure 9. C-Scan of failed Laminate-1 specimen [11].

(a) Microdamage $\frac{S_r}{S_r^{max}}$.

(b) Matrix shear failure D_{II}^m.

Figure 10. Normalized matrix microdamage contour $\frac{S_r}{S_r^{max}}$ and Matrix shear failure D_{II}^m in Laminate-1 at $P = 16{,}400$ lbf..

this behavior. The model exhibits slightly more strain, for a given load, prior to ultimate failure. At Sg-3, the model predicts strain localization after the ultimate load is achieved. The gage data shows a slight reduction in strain as the load drops; however, the gage was placed directly in the crack path and may have been damaged when the panel failed. The model results and experimental data for Sg-4 exhibit similar trends, but the strain gage shows a large degree of nonlinearity at the notch tip. This observed nonlinearity was attributed to local interlaminar stresses near the notch free edge which caused some local delaminations [11]. Since the focus of this work was modeling in-plane damage mechanisms, these effects are not captured; however, the model could be easily extended to incorporate delamination by placing DCZM elements between continuum shell layers [12].

A photograph taken of the failed, Laminate-2 specimen is presented in Figure 13. The photograph shows that two macroscopic cracks initially propagate from the notch tip towards the free edges, perpendicular to the applied load, in a self-similar fashion. Eventually, the cracks turn and proceed towards the free edge at an angle. [11] claim, supported by visual image correlation displacement data, that there was some eccentricity in the specimen alignment, which resulted in deviation from self-similar crack growth.

Contours representing the normalized microdamage in the 45° layer is presented in Figure 14 after the panel has completely failed and lost all of its load carrying capability. Although further matrix microdamage evolution is pro-
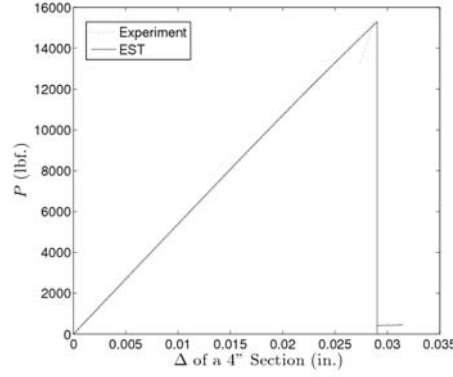
Figure 11. Applied load versus displacement of a 4" section for Laminate-2.

hibited in elements that have failed (transverse/shear or axial), in the other elements that have not failed, matrix microdamage evolution continues. Nearly the entire 45° and -45° layers reach a normalized microdamage level of 0.18. The 0° and 90° (not shown) plies exhibitted similar microdamage patterns; however, low levels of microdamage were more widespread in the 90° ply.

Figure 15a shows the fiber failure path once the specimen has completely failed. All of the layers, except the 90° layer (not shown), show self similar cracks propagating from the notch tips towards the free edges of the panel. The angled crack path shown in Figure 13 was not reproduced because the eccentric loading (suspected in the test) was not introduced into the simulation; therefore, the crack growth remained self-similar.

A high degree of transverse matrix failure can be seen in the axial crack path in the 45° ply in Figure 15b. This is also observed in the other plies, except the 0° layer. Finally, D_{II}^m is presented after the specimen has failed in Figure 15d. A highly degraded region has localized in the axial crack path.

CONCLUSION

A thermodynamically-based, work potential theory for damage and failure in composite materials, referred to as enhanced Schapery theory (EST), was developed. A marked distinction between damage and failure was introduced. Damage was considered to be the evolution of mechanisms that cause structural changes in the material such that the non-linear tangent stiffness tensor remains positive definite. Failure was taken to be the effect of structural changes in the material that result in loss of positive definiteness of the tangent stiffness matrix and post-peak strain softening.

Separate internal state variables (ISVs) were used to account for damage and three in-plane failure mechanisms. The relationship between the transverse and shear moduli of the lamina were related to the microdamage ISV through a pair of experimentally-obtainable microdamage functions. Evolution of the failure ISVs is based upon traction-separation laws (which are a functions of the appropriate fracture toughnesses) and a characteristic element length. No

(a) Sg-1.
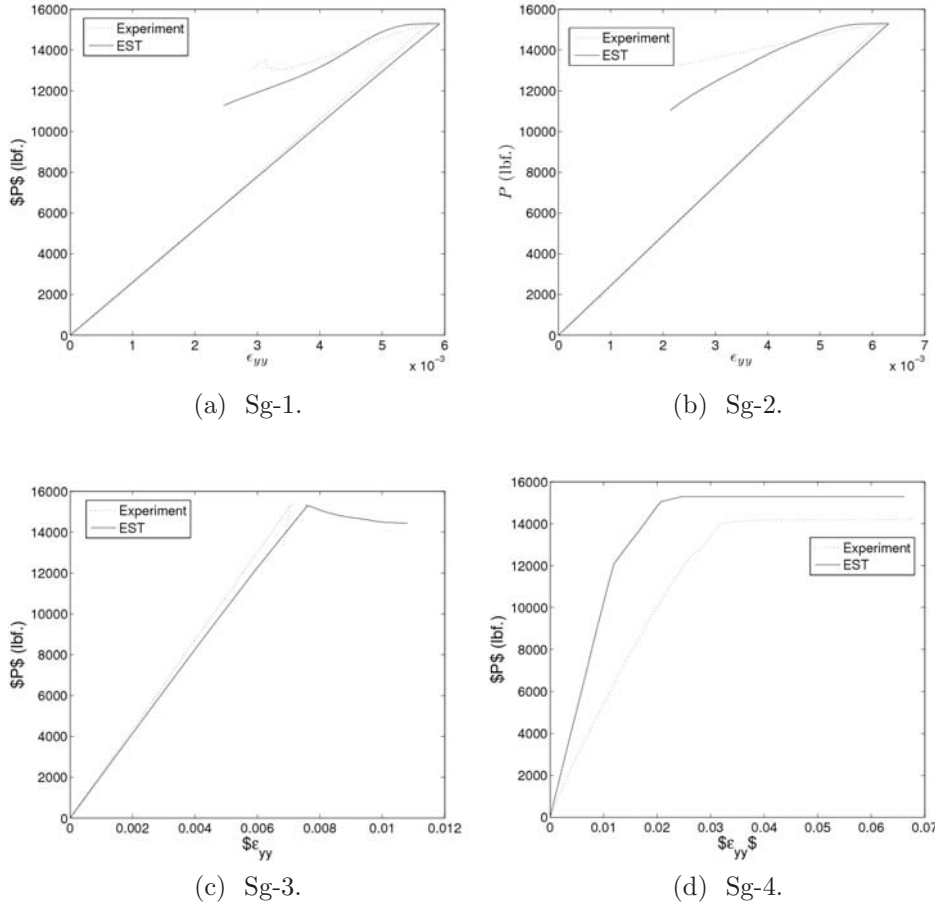
(b) Sg-2.

(c) Sg-3.

(d) Sg-4.

Figure 12. Applied load versus local strain for Laminate-2.

mixed-mode law is used to couple mode I and mode II failure, but one can be readily implemented. Typically, the existence of a non-positive definite stiffness tensor would result in pathologically mesh dependent solutions; however, in EST, mesh objectivity is ensured by incorporating a characteristic length scale into the failure evolution.

Two center-notched panels composed of T800/3900-2 were tested under tensile loading at NASA LaRC. Global load versus displacement and global load versus local strain gage strain data were compared to results obtained from FEM models utilizing EST. A single data point from each laminate was used to calibrate the EST failure parameters, and very good correlation was achieved for both laminates. The remaining strain gage and/or load-deflection results obtained from the EST simulations represent predictions and matched well with experimental data. Furthermore, damage and failure paths predicted by the models corresponded with the experimental results for both laminates examined. This lends confidence to the approach presented in this paper for predicting acreage damage and failure of laminated composite structures.
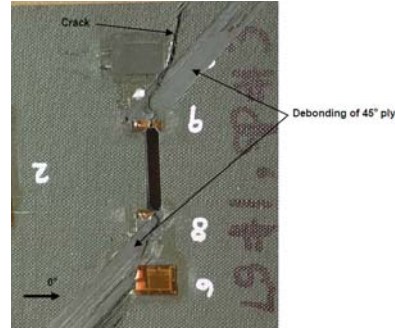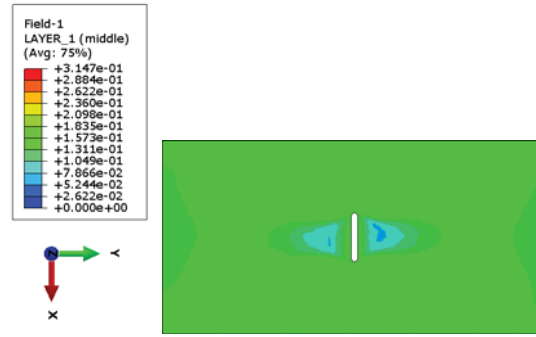
Figure 13. Photograph of failed Laminate-2 specimen [11].

(a) 45° Layer.

Figure 14. Normalized matrix microdamage contour $\frac{S_r}{S_r^{max}}$ in 45° layer of Laminate-2 after specimen has lost load carrying capability.
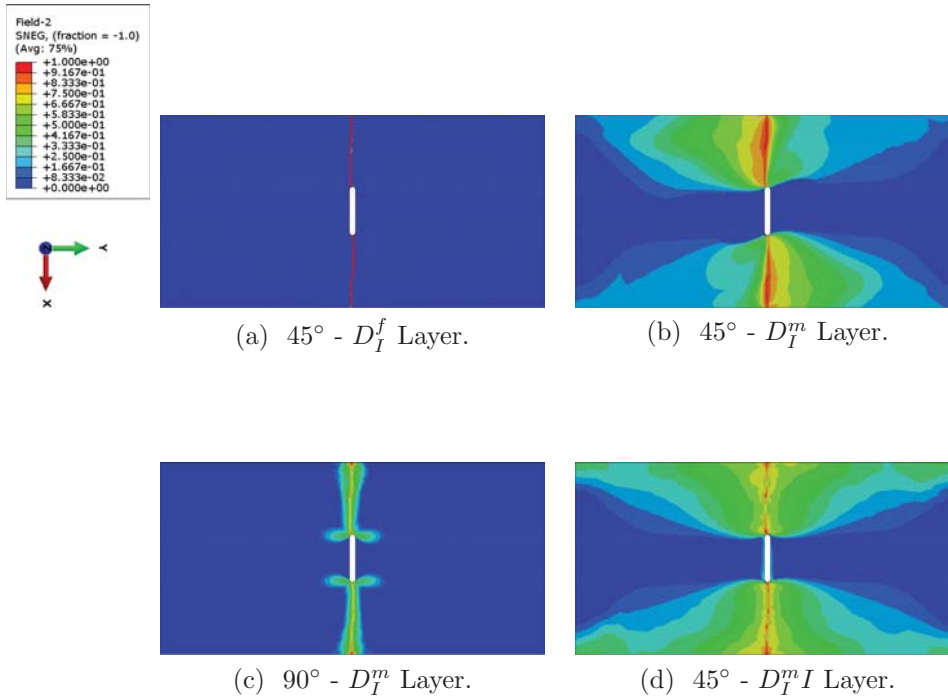

(a) 45° - D_I^f Layer.

(b) 45° - D_I^m Layer.

(c) 90° - D_I^m Layer.

(d) 45° - $D_I^m I$ Layer.

Figure 15. Failure in selected plies Laminate-2 after specimen has lost load carrying capability.

REFERENCES

1. Lamborn, M. J., R. A. Schapery. 1988."An Investigation of Deformation Path-Independence of Mechanical Work in Fiber-Reinforced Plastics," in *Proceedings of the Fourth Japan-U.S. Conference on Composite Materials,* Lancaster, PA: Technomic Publishing Co., Inc., pp. 991-1000.
2. Schapery, R. A. 1989. "Mechanical Characterization and Analysis of Inelastic Composite Laminates with Growing Damage," Mechanics & Materials Center Report 5762-89-10, Texas A & M University, College Station, TX 77804.
3. Schapery, R. A. 1990. "A Theory of Mchanical Behaviour of Elastic Media with Growing Damage and Other Changes in Structure," *J. Mech. Phys. Solids*, 38(2):1725–1797.
4. Lamborn, M. J., R. A. Schapery. 1993. "An Investigation of the Existence of a Work Potential for Fiber-Reinforced Plastic," *J. Compos. Mater.*, 27:352–382.
5. Sicking, D. L. 1992. "Mechanical Characterization of Nonlinear Laminated Composites with Transverse Crack Growth," PhD Thesis, Texas A&M University, College Station, TX.
6. Schapery, R. A., D. L. Sicking. 1995. "A Theory of Mechanical Behaviour of Elastic Media with Growing Damage and Other Changes in Structure," in *Mechanical Behaviour of Materials*, A. Bakker, eds. Delft, The Netherlands: Delft University Press, pp. 45–76.
7. Pineda, E. J., A. M. Waas, B. A. Bednarcyk, C. S. Collier. 2010. "Computational Implementation of a Thermodynamically Based Work Potential Model for Progressive Microdamage and Transverse Cracking in Fiber-Reinforced Laminates," presented at the 51st AIAA/ASME/ASCE/AHS/ASC Structures, Structural Dynamics, and Materials Conference, Orlando, FL, April 12–15, 2010.
8. Bažant, Z. P., B. H. Oh. 1983. "Crack Band Theory for Fracture of Concrete," *Mater. and Struct.*, 16:155–77.
9. Rots, J. G., R. deBorst. 1987. "Analysis of Mixed-Mode Fracture in Concrete," *J. Eng. Mech.*, 113(11):1739–1758.
10. Talreja, R. 1985. "Transverse Cracking and Stiffness Reduction in Composite Laminates," *J. Composite Materials*, 19:355–275.
11. Bogert, P. B., A. Satyanarayana, P. B. Chunchu. 2006. "Comparison of Damage Path Predicions for Composite Laminates by Explicit and Standard Finite Element Analysis Tool," presneted at 47th AIAA Structures, Structural Dynamics, and Materials Conference, Newport, RI, May 1–4, 2006.
12. A. Satyanarayana, P. B. Bogert, P. B. Chunchu. 2007. "The Effect of Delamination on Damage Path and Failure Load Prediction for Notched Composite Laminates," presented at 48th AIAA Structures, Structural Dynamics, and Materials Conference, Honolulu, HI, April 23–26, 2007.
13. Schapery, R. A. 1995. "Prediction of Compressive Strength and Kink Bands in Composites Using a Work Potential," *Int. J. Solids Structures*, 32(6):739–765.
14. Basu, S., A. M. Waas, D. R. Ambur. 2006. "Compressive Failure of Fiber Composites Under Multiaxial Loading," *J. Mech. Phys. Solids*, 54(3):611–634.
15. Pineda, E. J., A. M. Waas, B. A. Bednarcyk, C. S. Collier, P. W. Yarrington. 2009. "Progressive Damage and Failure Modeling in Notched Laminated Fiber Reinforced Composites," *Int. J. Fract.*, 158:125–143.
16. Pineda, E. J., A. M. Waas. 2011. "Numerical Implementation of a Multiple-ISV Thermodynamically-Based Work Potential Theory for Modeling Progressive Damage and Failure in Fiber-Reinforced Laminates," *NASA/TM 2011-217401*
17. Pineda, E. J., A. M. Waas. 2012. "Modelling Progressive Failure of Fibre Reinforced Laminated Composites: Mesh Objective Calculations," *Aeronaut. J.*, 116(1186):1221–1246.
18. Pineda, E. J., A .M. Waas. 2013. "Mesh Objective Implementation of a Thermodynamically-Based Work Potential Theory for Modeling Progressive Damage and Failure in Fiber-Reinforced Laminates," *Int. J. Fract.*, in press.
19. Hinterhoelzl, A., R. A. Schapery. 2004. "FEM Implementation of a Three-Dimensional

Visoelastic Constitutive Model for Particulate Composites with Damage Growth," *Mech. Time-Depend. Mat.*, 8(1):65–94.

20. Rice, J. R. 1971. "Inelastic Constitutive Relations for Solids: an Internal-Variable Theory and its Application to Metal Plasticity," *J. Mech. Phys. Solids*, 19:433–455.

21. Song, S. J., A. M. Waas. 1995. "An Energy Based Model for Mixed Mode Failure of Laminated Composites," *AIAA Journal*, 33(4):739–745.

22. Ortiz, M., A. Pandolfi. 1999. "Finite-Deformation Irreversible Cohesive Elements for Three Dimensional Crack-Propagation Analysis," *Int. J. Numer. Meth.*, 44:1267–1282.

23. Ji, W., A. M. Waas. 2013. "Progressive Failure Analysis for the Interaction of Interlaminar and Intralaminar Failure Modes in Composite Structures with an Initial Ddelamination," *Aeronaut. J.*, 117(1187):109–129.

24. Lemaitre, J., J.-L. Chaboche. 1994. *Mechanics of Solid Materials*, Cambridge: Cambridge University Press.

25. Matzenmiller, A., J. Lubliner, R. L. Taylor. 1995. "A Constitutive Model for Anisotropic Damage in Fiber-Composites," *Mech. Mater.*, 20(2):125–152.

26. Lemaitre, J. 1996. *A Course on Damage Mechanics, 2nd Ed.*, Berlin, Heidelberg, New York: Springer-Verlag.

27. Camanho, P. P., P. Maimí, C. G. Dávila. 2007. "Prediction of Size Effects in Notched Laminates Using Continuum Damage Mechanics," *Compos. Sci. and Technol.*, 67:2715–2727.

28. Maimi, P., Camanho, P. P., Mayugo, J. A., and Dávila, C. G. 2007. "A continuum damage model for composite laminates: Part I - Constitutive model," *Mechanics of Materials* **39**, 897–908.

29. Schuecker, C., H. E. Pettermann. 2008. "Fiber Reinforced Laminates: Progressive Damage Modeling Based on Failure Mechanisms," *Arch. Comput. Methods Eng.*, 15:163–184.

30. Bednarcyk, B. A., J. Aboudi, S. M. Arnold. 2010. "Micromechanics Modeling of Composites Subjected to Multiaxial Progressive Damage in the Constituents," *AIAA J.*, 48: 1367–1378.

31. Hashin, Z. A. Rotem. 1973. "A Fatigue Failure Criterion for Fiber Reinforced Composite Materials," *J. Composite Materials*, 7:448–464.

32. Barenblatt, G. I. 1962. "The Mathematical Theory of Equilibrium Cracks in Brittle Fracture," *Adv. Appl. Mech.*, 7:55–129.

33. Xie, D. E., A. Salvi, C. E. Sun, A. M. Waas, A. Caliskan. 2006. "Discrete Cohesive Zone Model to Simulate Static Fracture in 2-D Triaxially Braided Carbon Fiber composites," *J. Compos. Mater.*, 40(22):2025–2046.

34. Gustafson, P. A. 2008. "Analytical and Experimental Methods for Adhesively Bonded Joints Subjected to High Temperatures," PhD Thesis, University of Michigan, Ann Arbor, MI.

35. Turon, A., P. P. Camanho, J. Costa, C. G. Dávila. 2006. "A Damage Model for the Simulation of Delamination in Advanced Composites Under Variable-Mode Loading," *Mech. Mater.*, 38(11):1072–1089.

36. Jones, R. M. 1999. *Mechanics of Composite Materials, 2nd Ed.*, Philadelphia, PA: Taylor and Francis, Inc.

37. Abaqus. 2008. *Abaqus User's Manual, Vol. 1-3, Version 6.10-1* Providence, RI: Dassault Systèmes Simulia Corp.

38. Camanho, P. P., C. G. Dávila, S. T. Pinho, L. Iannucci, P. Robinson. 2006. "Prediction of in Situ Strenghts and Matrix Cracking in Composites Under Transverse Tension and in-Plane Shear," *Composites: Part A*, 37:165–176.